

# ISS Policy : Scalable Diffusion Policy with Implicit Scene Supervision

Wenlong Xia\*, Jinhao Zhang\*, Ce Zhang, Yaojia Wang, Youmin Gong and Jie Mei<sup>‡</sup>

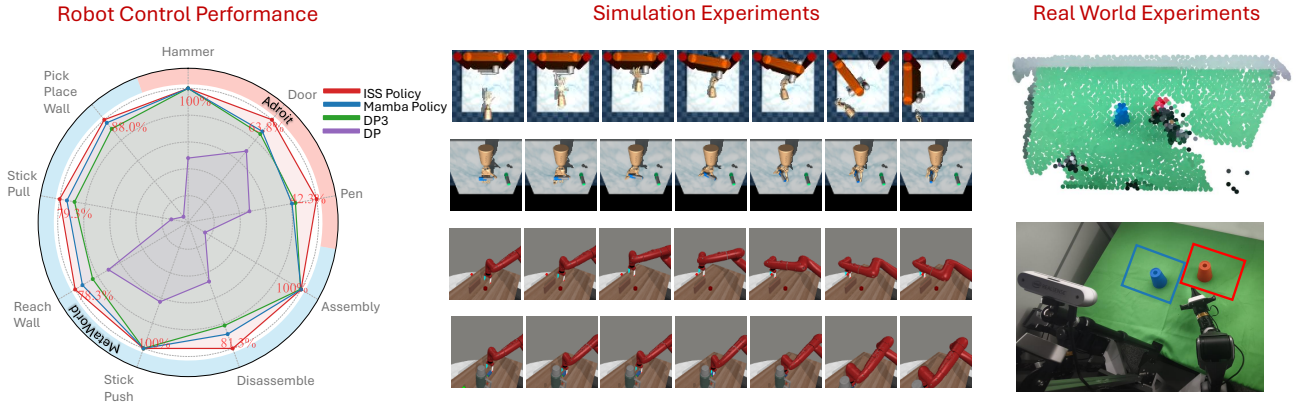


Fig. 1: **ISS Policy** is a novel 3D visuomotor diffusion-based policy that generates continuous action sequences from point cloud inputs. It exhibits strong scalability and learning efficiency, achieving state-of-the-art performance on challenging simulation benchmarks and demonstrating strong robustness in real-world experiments.

**Abstract**—Vision-based imitation learning has enabled impressive robotic manipulation skills, but its reliance on object appearance while ignoring the underlying 3D scene structure leads to low training efficiency and poor generalization. To address these challenges, we introduce *Implicit Scene Supervision (ISS) Policy*, a 3D visuomotor DiT-based diffusion policy that predicts sequences of continuous actions from point cloud observations. We extend DiT with a novel implicit scene supervision module that encourages the model to produce outputs consistent with the scene’s geometric evolution, thereby improving the performance and robustness of the policy. Notably, ISS Policy achieves state-of-the-art performance on both single-arm manipulation tasks (MetaWorld) and dexterous hand manipulation (Adroit). In real-world experiments, it also demonstrates strong generalization and robustness. Additional ablation studies show that our method scales effectively with both data and parameters. Code and videos will be released.

## I. INTRODUCTION

Visuomotor policies, which map high-dimensional visual observations directly to low-level actions, are pivotal for enabling robots to perform complex tasks in unstructured environments [1], [2]. Imitation Learning (IL) from expert demonstrations has emerged as a robust and scalable paradigm for acquiring these skills. By directly leveraging expert supervision, IL enables robots to master intricate behaviors ranging from navigation [3] to dexterous manipulation [4].

Despite these successes, generalization in imitation learning heavily relies on the availability of large-scale demonstrations [5], [6]. However, data containing precise object states, such as 6D poses and contact forces, is scarce and expensive to acquire, often necessitating specialized sensors and tedious calibration processes. Consequently, to scale learning across diverse environments, the community has largely converged on utilizing raw visual observations, such as RGB images or

depth maps, as the primary input modality. Given reliance on visual observations, the choice of input representation becomes a critical determinant of policy performance. Many works, including Implicit Behavior Cloning (IBC) [6] and BC-RNN [7], perform end-to-end learning directly from 2D images. However, the lack of depth in 2D policies creates spatial ambiguity, limiting performance in tasks with occlusions or fine-grained contact that require precise geometric reasoning [8].

To mitigate 2D limitations, recent research has incorporated 3D representations [9], [8], which provide rich geometric context to improve manipulation performance. However, existing 3D-based policies typically use heavy network architectures [10], which make inference slow and computationally expensive [11]. Moreover, they solely rely on the policy loss to provide supervision for both scene encoder and action head, which is too weak and indirect, leading to poor learning efficiency. In contrast, providing the policy with additional 3D scene prediction and view-synthesis tasks as geometric supervision during training has been shown to significantly improve the quality of the learned scene representations and the resulting control performance [12].

To this end, we propose **ISS Policy**, a novel 3D visuomotor policy designed to handle both high-dimensional and low-dimensional control tasks with high efficiency and robustness. We convert single-view depth into sparse point clouds and feed them to a conditional diffusion model [13] to produce continuous action sequences. Notably, we introduce an Implicit Scene Supervision (ISS) module. This auxiliary module predicts future point cloud features to enforce long-term geometric consistency, enabling the policy to implicitly model scene dynamics and improve the model’s spatial rea-

soning ability, thereby yielding richer spatial-semantic representations and significantly improving learning efficiency.

We evaluate our approach across challenging simulation tasks and real-world manipulation scenarios. Our results demonstrate that the proposed policy exhibits superior robustness, scalability, and learning efficiency compared to state-of-the-art 2D and 3D baselines.

Our contributions can be summarized as follows:

- We propose a DiT-based 3D visuomotor policy for robotic manipulation that is highly training-efficient and exhibits favorable scalability with respect to both model size and dataset size.
- We introduce a novel *implicit scene supervision* loss that provides an additional implicit dynamics-aware constraint on the model’s outputs, enforcing long-term geometric consistency in its predictions.
- Our method achieves state-of-the-art performance on dexterous hand manipulation (Adroit) and diverse single-arm manipulation tasks (MetaWorld), while enjoying a more efficient and stable training process.

## II. RELATED WORKS

### A. Visuomotor Imitation Learning

Imitation learning from expert demonstrations has emerged as a powerful paradigm for acquiring robotic manipulation skills [14], [7]. Numerous works have explored end-to-end imitation learning directly from 2D visual observations, mapping RGB images to actions with convolutional or transformer-based policies [5], [6], [15], [16], [17], [18]. While these methods prove simple and effective on standard benchmarks, their inherent lack of depth and 3D geometry often results in brittle behavior during fine-grained, multi-object, and long-horizon manipulation tasks [19], [20].

This realization has spurred a shift towards 3D-aware policies leveraging explicit geometric representations [21], [8], [10], [22], [9], [23]. While methods based on dense voxel grids [9], [10] or continuous 3D feature fields [21], [22], [23] offer rich spatial details, they are often compute-intensive, limiting training scalability and inference speed. Conversely, a more efficient alternative is to use a sparse point-cloud encoder, as introduced in DP3 [8]. Building upon this efficiency, we propose a streamlined policy that operates on point clouds from single-view depth maps. To further enhance geometric reasoning without incurring inference overhead, we augment the policy with an implicit scene supervision head that predicts future feature.

### B. Diffusion Models for Robotics

Diffusion models are a class of generative models that transform random noise into complex data through a gradual denoising process, and were popularized for high-fidelity image synthesis [13], [24], [25], [26].

As diffusion models matured beyond image synthesis, the community began applying them to decision making and robotic control. Diffusion Policy [5] first established the paradigm of representing policies as conditional diffusion processes. This paradigm has subsequently seen widespread

adoption across a broad spectrum of tasks, including general manipulation [22], [27], [28], [29], grasping [30], [31], [32], [33], and navigation [34], [35], [36]. To further enhance expressiveness and scalability, RDT [17] introduced the Diffusion Transformer (DiT) [37] backbone to robotic manipulation, demonstrating the superiority of DiT in handling heterogeneous robotic data. Leveraging the superior scalability and computational efficiency of DiT, we design a specialized policy architecture tailored for robotic manipulation with point clouds input, to generate precise action sequences.

## III. PRELIMINARIES

### A. Diffusion Models

The basic idea of Denoising Diffusion Probabilistic Models (DDPM) [13] is to construct a simple forward diffusion process that progressively destroys structure in the data by adding noise, and then learn a reverse process that reconstructs clean data from noisy inputs.

**Forward Diffusion.** The forward process defines a sequence  $\{x_t\}_{t=1}^T$  by repeatedly adding Gaussian noise according to a Markov chain:

$$q(\mathbf{x}_t|\mathbf{x}_{t-1}) = \mathcal{N}(\mathbf{x}_t; \sqrt{1 - \beta_t}\mathbf{x}_{t-1}, \beta_t\mathbf{I}), \quad t = 1, \dots, T, \quad (1)$$

where  $\{\beta_t\}_{t=1}^T$  is a predefined variance schedule with  $\beta_t \in (0, 1)$ . Because the forward process is linear and Gaussian, one can also sample any intermediate state in closed form:

$$q(\mathbf{x}_t|\mathbf{x}_0) = \mathcal{N}(\mathbf{x}_t; \sqrt{\bar{\alpha}_t}\mathbf{x}_0, (1 - \bar{\alpha}_t)\mathbf{I}), \quad (2)$$

where  $\alpha_t = 1 - \beta_t$  and  $\bar{\alpha}_t = \prod_{s=1}^t \alpha_s$ . As  $t$  increases,  $x_t$  gradually converges to standard Gaussian.

**Reverse Denoising.** The reverse process begins by sampling  $x_T \sim \mathcal{N}(0, \mathbf{I})$  and iteratively recover the original data  $x_0$ . The exact reverse conditionals  $q(x_{t-1}|x_t)$  are intractable, so they are approximated by a parameterized Gaussian

$$p_\theta(\mathbf{x}_{t-1}|\mathbf{x}_t) = \mathcal{N}(\mathbf{x}_{t-1}; \boldsymbol{\mu}_\theta(\mathbf{x}_t, t), \boldsymbol{\Sigma}_\theta(\mathbf{x}_t, t)), \quad (3)$$

where a neural network estimates either the mean  $\mu_\theta$  or equivalently the noise contained in  $x_t$ . In DDPM, the variance is typically fixed as a function of the schedule, and the network  $\epsilon_\theta(x_t, t)$  is trained to predict the true noise  $\epsilon$  used to construct  $x_t$ . The objective reduces to a simple mean-squared error

$$\mathcal{L}_{\text{ddpm}} = \mathbb{E}_{t, \mathbf{x}_0, \epsilon} \left[ \|\epsilon - \epsilon_\theta(\sqrt{\bar{\alpha}_t}\mathbf{x}_0 + \sqrt{1 - \bar{\alpha}_t}\epsilon, t)\|_2^2 \right], \quad (4)$$

which can be interpreted as a variational bound on the negative log-likelihood.

In this work, we adopt the DDPM formulation as the underlying diffusion framework and employ DDIM-style sampling to obtain efficient and high-quality generations within our proposed policy architecture.

## IV. METHOD

As illustrated in Fig. 2, we propose a DiT-based policy with implicit scene supervision for visuomotor control from single-view 3D point clouds. The architecture has two main components: (i) a DiT-based module that generates future

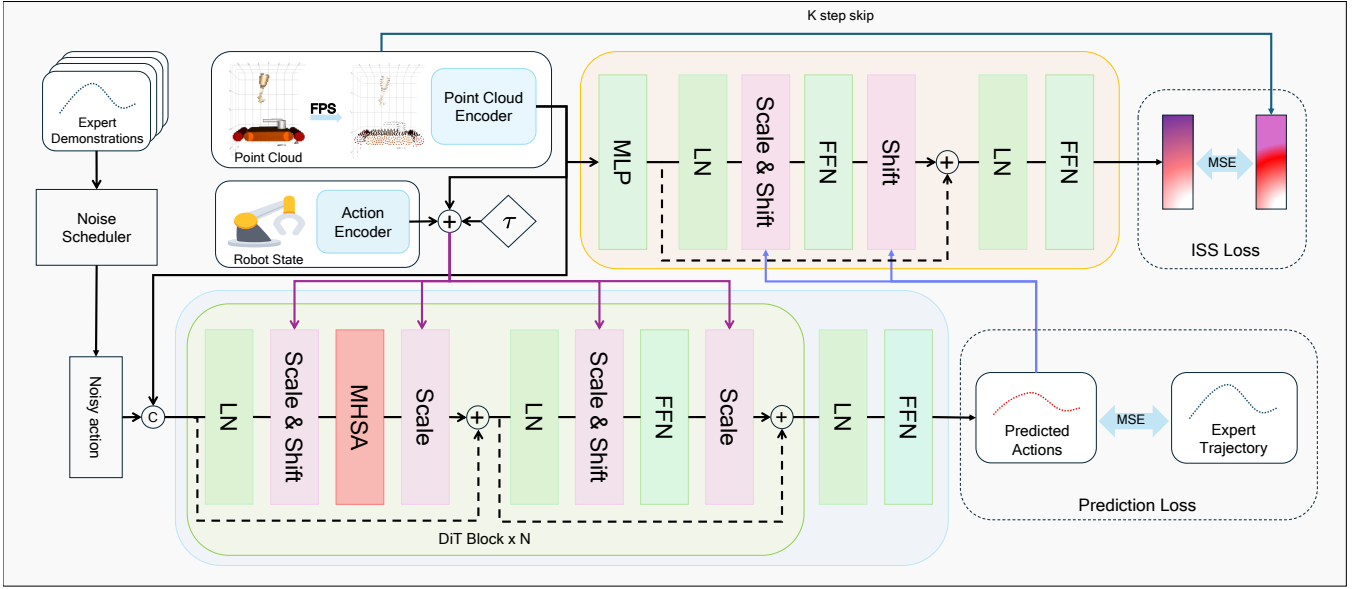


Fig. 2: **Model Architecture of ISS Policy.** Expert demonstrations of point clouds and robot states are first encoded into observation context. During training, a diffusion noise scheduler adds noise to expert action trajectories, and a DiT-based policy head conditions on the context and diffusion timestep  $t$  to denoise them and predict future action sequences. After the DiT policy produces a candidate trajectory, an implicit scene supervision (ISS) head takes the global point-cloud context together with a length- $K$  subsequence of predicted actions and predicts a skip-step future point-cloud embedding, providing an auxiliary future prediction signal that shapes the learned representations during training.

actions conditioned on the history of observations, and (ii) a prediction head that forecasts skip-step future point-cloud embeddings, providing implicit geometric dynamic supervision during training. The problem formulation and model details are presented below.

### A. Problem Formulation

We assume access to a dataset of expert demonstrations

$$\mathcal{D} = \{(\mathbf{O}_t, \mathbf{A}_t)\} \quad \mathbf{O}_t = (\mathbf{P}_t, \mathbf{s}_t) \quad (5)$$

$\mathbf{O}_t$  denotes the observation, and  $\mathbf{A}_t$  is the corresponding expert action. Each observation consists of the single-view, robot-centric point clouds  $\mathbf{P}_t$  and proprioceptive states  $\mathbf{s}_t$ .

During training and deployment, we operate on fixed-length windows extracted from these trajectories. Following Diffusion Policy [5], we distinguish three temporal quantities as shown in Fig. 3: the total prediction horizon  $T$ , the observation window length  $T_o$ , and the number of action steps to execute  $T_a$ , with  $T_a \leq T$ . Our goal is to learn an end-to-end visuomotor policy  $\pi_\theta : \mathcal{O}^{T_o} \rightarrow \mathcal{A}^T$  parameterized by  $\theta$ , where  $\mathcal{O}$  and  $\mathcal{A}$  denote the per-timestep observation space and action space, respectively. At execution time, however, only the first  $T_a$  actions are applied to the robot in a receding-horizon manner.

### B. DiT Architecture

Our DiT architecture follows an encoder-decoder design. The encoder encodes the point clouds and robot states into context representations  $z_{pc}$  and  $z_{state}$ , respectively. The decoder takes as input the noisy action sequence  $\mathbf{A}_t^{(\tau)}$  together with the context and decodes the corresponding

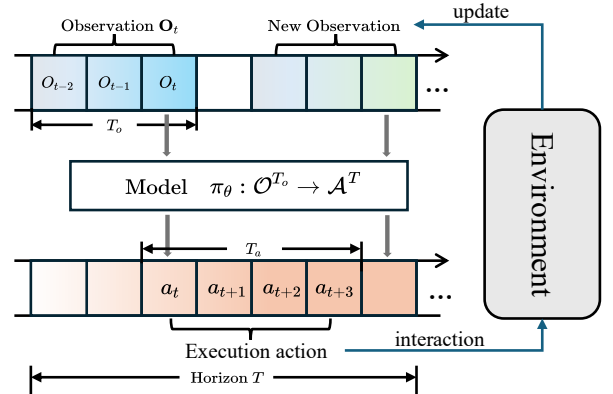


Fig. 3: **Policy Formulation.**

clean data [38], where  $\tau \in [0, 1]$  is the diffusion timestep. The detailed architectural design is described below.

**Condition Encoder.** Following DP3 [8], we use Multi-layer perceptrons (MLPs) with a max-pooling operation as the point cloud encoder:

$$z = \text{maxpool}[\text{MLP}(\mathbf{P}_t)] \quad (6)$$

$$z_{pc} = \text{MLP}(z) \quad (7)$$

where  $\mathbf{P}_t$  is the point clouds input at frame  $t$ . This simple model efficiently encodes sparse point clouds into compact, information-dense representations. For the robot states, we directly encode them with an MLP:

$$z_{state} = \text{MLP}(\mathbf{s}_t) \quad (8)$$

**Action Decoder.** The action decoder, responsible for predicting clean actions from noisy data, follows a standard DiT [37] architecture. Specifically,  $\mathbf{A}_t^{(\tau)}$  is first embedded into a high-dimensional space to obtain an embedding  $H \in \mathbb{R}^{T \times D}$ , where  $D$  is embedding dimension. To enhance the spatial awareness of the denoising process, we fuse the noisy embedding  $H$  with the point cloud features  $z_{pc}$  to obtain the action query  $Q \in \mathbb{R}^{T \times D}$ :

$$Q = \text{MLP}(\text{concat}(H, z_{pc})). \quad (9)$$

Then, in each DiT block, multi-head self-attention [39] and AdaLN-zero [37] are used to perform temporal interaction and condition injection, respectively:

$$Q = Q + \text{MHSA}(\text{AdaLN}(Q, C)) \quad (10)$$

$$Q = Q + \text{FFN}(\text{AdaLN}(Q, C)) \quad (11)$$

where  $C = z_{pc} + z_{\text{state}} + \text{Emb}(\tau)$  serves as the denoising condition and  $\text{Emb}(\tau)$  denotes the sinusoidal positional embedding of the diffusion timestep  $\tau$ . After passing through  $N$  such blocks, a final prediction head is applied to predict the target action.

### C. Implicit Scene Supervision

As mentioned in [40], if the actions output by the model are correct, they should enable accurate prediction of the corresponding future scene. Inspired by this, we introduce an additional implicit supervision signal for the predicted actions via scene prediction: given the current scene and the predicted actions, we predict the future scene and use the prediction error as an auxiliary loss term.

As illustrated in Fig. 2, we leverage the action sequence predicted by action decoder to forecast future point cloud scenes. Rather than predicting the point cloud of the next frame, we choose to predict the scene  $K$  steps into the future. This is because adjacent point clouds often differ only slightly, making it difficult for the model to extract informative supervision from such small geometric changes. While predicting a farther future frame encourages the model to capture more meaningful long-range dynamics and object motion. Formally, given the encoded point cloud  $z_{pc,t}$  at the current timestep and the predicted action sequence  $\hat{\mathbf{A}}_{t,K} = \hat{a}_{t:t+K}$ , we construct a scene prediction module composed of several feed-forward networks and adaptive layer normalization:

$$z = \text{MLP}(z_{pc,t}) \quad (12)$$

$$z = z + \text{FFN}(\text{AdaLN}(z, \hat{\mathbf{A}}_{t,K})) \quad (13)$$

$$\hat{z}_{pc,t+K} = z + \text{FFN}(z) \quad (14)$$

where  $\hat{z}_{pc,t+K}$  denotes the predicted point cloud representation  $K$  steps into the future and AdaLN is employed to inject action information into the prediction model.

The implicit scene supervision objective is a simple self-supervised regression loss in the point-cloud embedding space:

$$\mathcal{L}_{\text{iss}} = \mathbb{E} \left[ \left\| \hat{z}_{pc,t+K} - z_{pc,t+K} \right\|_2^2 \right]. \quad (15)$$

Importantly, this supervision requires no additional labels beyond the demonstration trajectories themselves: both the input (historical point clouds and actions) and the target (future point cloud) are directly available from the data. By forcing the policy to produce action sequences that are consistent with the predicted future geometry of the scene, the implicit scene supervision head shapes the internal representations toward capturing longer-horizon 3D dynamics, which empirically improves generalization to out-of-distribution configurations. Besides, the prediction branch is only used during training and is discarded at test time, so it does not increase inference cost.

Considering the inevitable mismatch between the predicted actions and the ground truth during training, directly supervising the scene predictor with the future point cloud corresponding to the ground-truth actions can lead to training instability, especially in the early stages before convergence. Therefore, to stabilize learning and avoid error accumulation at early training stages, we use the ground-truth actions with probability  $p$  when predicting the future point cloud. Formally, the action input to the scene predictor is modified as:

$$\tilde{\mathbf{A}}_{t,K} = \begin{cases} \mathbf{A}_{t,K}, & \text{with probability } p, \\ \hat{\mathbf{A}}_{t,K}, & \text{with probability } 1 - p. \end{cases} \quad (16)$$

This strategy is analogous to scheduled sampling [41] and helps alleviate the exposure bias caused by the mismatch between model predictions and ground-truth actions.

### D. Training Objective

We adopt a standard denoising diffusion objective for action modeling:

$$\mathcal{L}_{\text{bc}} = \mathbb{E}_{\tau \sim (0,1), \mathbf{A}_t^{(0)}, \mathbf{A}_t^{(\tau)} \sim q(\mathbf{A}_t^{(\tau)} | \mathbf{A}_t^{(0)})} \left[ \left\| \hat{\mathbf{A}}_t^{(0)} - \mathbf{A}_t^{(0)} \right\|_2^2 \right] \quad (17)$$

The overall training objective is a weighted sum of denoising loss and implicit scene supervision loss:

$$\mathcal{L}(\theta, \psi) = \mathcal{L}_{\text{bc}}(\theta) + \lambda_{\text{iss}} \mathcal{L}_{\text{iss}}(\theta, \psi), \quad (18)$$

where  $\theta$  denotes the parameters of the DiT policy (including the observation encoders) and  $\psi$  denotes the parameters of the ISS head. The coefficient  $\lambda_{\text{iss}} > 0$  controls the strength of implicit scene supervision. At test time, the ISS head is discarded and only the DiT policy is used to generate action sequences.

## V. EXPERIMENTS

**Simulation Benchmark.** Simulation benchmarks play a crucial role in evaluating visuomotor policies before deployment on physical robots. We evaluate our approach on simulated manipulation tasks from the Adroit [42] and MetaWorld [43] benchmarks. Adroit focuses on dexterous hand manipulation with high-dimensional continuous control, offering a challenging testbed for precise, long-horizon skills. MetaWorld provides a diverse set of single-arm manipulation tasks (e.g., pushing, picking, placing) categorized into multiple difficulty levels following prior work [44]. The 3D observations are visualized in Figure 4.

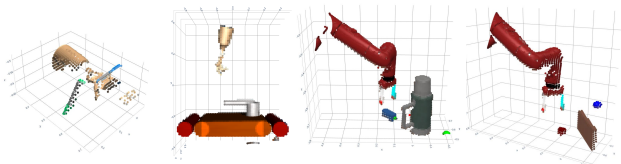


Fig. 4: **Visualization of 3D point-cloud observations in simulation environments.** We show representative 3D point clouds from Adroit and MetaWorld.

**Expert Demonstrations.** For the Adroit tasks, we collect successful trajectories using reinforcement learning (RL) agents trained with VRL3 [45], which has been shown to produce strong expert policies in dexterous manipulation domains. For MetaWorld tasks, we follow the standard protocol and use built-in scripted policies to generate expert demonstrations. In all cases, we only retain successful rollouts and use them as expert demonstrations for imitation learning.

**Baselines.** Our goal is to highlight the benefits of our proposed architecture, so our main baseline is the 3D-based policy DP3 [8], which represents the current SOTA in point cloud conditioned policies. In addition, we include the 2D-based policy DP [5], IBC [6] and BCRNN [7] and 3D-based policy Mamba Policy [28]. All baselines are trained on the same set of expert demonstrations as our method, and we match the image and depth resolutions across all 2D and 3D variants for fair comparison. Due to the limited effectiveness of these algorithms, we evaluate them only on 9 representative tasks (3 from Adroit and 6 from MetaWorld).

**Evaluation Metrics.** For each experiment, we train three runs with random seeds  $\{0,1,2\}$ . During training, we evaluate the policy every 200 epochs, and each evaluation consists of 20 rollouts per task, from which we obtain a success rate. For a given seed, we collect all success rates over the course of training, and define  $SR_5$  as the average of the top five. Finally, we report the mean and standard deviation of  $SR_5$  across the three seeds.

**Experiment Settings.** We set the prediction horizon to  $T = 4$ , with observation steps  $T_o = 2$  and action steps  $T_a = 3$ . Following DP3 [8], we use a DDIM noise scheduler with 100 diffusion steps during training and 10 steps at inference, and optimize with AdamW with an initial learning rate of  $1 \times 10^{-4}$  and a cosine decay schedule. Both actions and robot states are normalized to  $[-1, 1]$  before training, and actions are mapped back for execution. All models are trained for 3000 epochs with a batch size of 128. Our model and all baselines are trained and evaluated on a single NVIDIA RTX 5880 GPU.

#### A. Comparisons with the State-of-the-Arts

As shown in Tab. I, we compare ISS Policy with state-of-the-art visuomotor baselines on Adroit and MetaWorld in terms of  $SR_5$ . Classical behavior-cloning baselines such as BCRNN and IBC perform poorly (average  $SR_5 \leq 15\%$ ), suggesting that traditional behavior cloning with a unimodal

regression objective tends to suffer from mode averaging. In contrast, diffusion-based policies (Diffusion Policy, DP3, and Mamba Policy) substantially improve over these methods by modeling the multimodal structure of the action distribution. Among all methods, ISS Policy attains the highest average success rate, consistently outperforming both 2D and 3D diffusion baselines.

These substantial improvements on these tasks highlight the advantage of ISS Policy: by leveraging structured state-space modeling over 3D point-cloud observations, it better captures long-range temporal dependencies and achieves state-of-the-art performance among point-cloud-based visuomotor control methods.

#### B. Scalability Evaluation

We study how ISS Policy scales along two axes: the capacity of the DiT-based action head and the amount of demonstration data.

**Scaling with model capacity.** Table II and Fig. 6 vary the size of the DiT policy head from Small to Large. Across four tasks, larger DiT heads consistently lead to higher  $SR_5$ , and the gains are monotonic with model size. This indicates that our architecture can effectively exploit additional policy capacity rather than saturating at a small scale.

**Scaling with training data.** Table III varies the number of expert demonstrations while keeping the architecture fixed. ISS Policy already attains strong performance with only 10 demonstrations and improves steadily as more data are provided, with the largest gains on the more challenging Pen task. These trends show that ISS Policy is both data-efficient in the low-data regime and capable of benefiting from additional demonstrations when they are available.

#### C. Learning Efficiency and Stability

We further compare the training curves of ISS Policy against DP3. As shown in Fig. 5, ISS Policy consistently attains high performance much earlier in training than DP3. The success rate of ISS Policy increases sharply in the early training phase, whereas DP3 improves gradually and often requires substantially more epochs to reach comparable performance.

To quantitatively assess training stability, we examine the standard deviations reported in Tab. I. Averaged over all tasks, ISS Policy achieves an  $SR_5$  standard deviation of about 1.9 percentage points, which is noticeably lower than DP3 ( $\sim 3.2$ ) and Mamba Policy ( $\sim 2.7$ ). Our method exhibits lowest variance, while at the same time achieving the highest success rate. These results suggest that ISS Policy not only converges faster but also produces more consistent performance across different seeds.

#### D. Ablation Study

**Impact of Designed Module.** Table IV shows that conditional fusion yields modest gains by better grounding action queries in the 3D point-cloud context. However, adding ISS on top of fusion delivers only marginal improvements, because the auxiliary loss is supervised solely under predicted

TABLE I: **Quantitative comparisons of different baselines in simulation environments.** We compare our ISS Policy with BCRNN, IBC, Diffusion Policy, DP3, and Mamba Policy on simulation tasks in terms of SR<sub>5</sub>. Unavailable results for BCRNN and IBC are denoted by “-”. Results reproduced with the official code repository are denoted by \*.

Method	Adroit			MetaWorld						Average
	Hammer	Door	Pen	Assembly	Disassemble	Stick-Push	Reach-Wall	Stick-Pull	Pick-Place-Wall	
BCRNN	0±0	0±0	9±3	3±4	32±12	45±11	-	-	-	-
IBC	0±0	0±0	9±2	0±0	1±1	16±2	-	-	-	-
Diffusion Policy	48±17	50±5	25±4	15±1	43±7	63±3	59±7	11±2	5±1	35.4
DP3*	100.0±0.0	62±4	43.7±5.3	99.6±0.4	75.0±3.0	100.0±0.0	70.7±6.7	74.3±4.3	82.7±5	78.7
Mamba Policy*	100.0±0.0	63.8±7.8	42.3±5.2	100.0±0.0	81.3±3.7	100.0±0.0	78.3±4.3	79.3±1.3	88.0±2.0	81.4
<b>ISS Policy (Ours)</b>	<b>100.0±0.0</b>	<b>72.0±2.0</b>	<b>52.3±2.7</b>	<b>100.0±0.0</b>	<b>91.7±4.7</b>	<b>100.0±0.0</b>	<b>83.7±0.7</b>	<b>85.3±4.7</b>	<b>90.7±1.9</b>	<b>86.2</b>

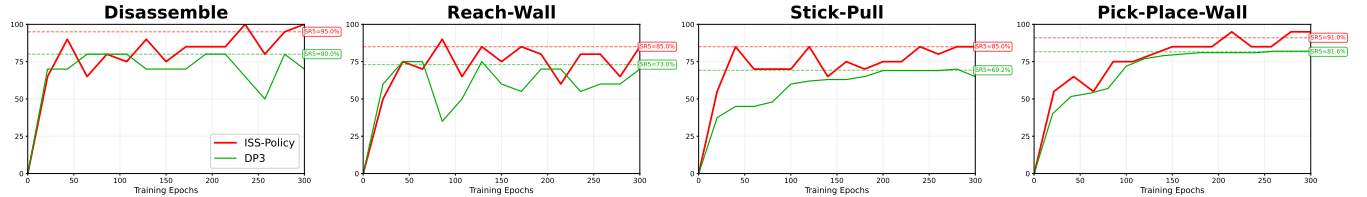


Fig. 5: **Learning Efficiency and Stability.** We plot training curves of ISS Policy and DP3 on MetaWorld tasks. The dashed horizontal lines denote the SR<sub>5</sub> metric. Across all tasks, ISS Policy achieves higher success rates, higher learning efficiency, and better asymptotic performance.

TABLE II: **DiT configurations in the scalability study.** We consider three variants (Small, Medium, Large) with increasing depth, width, and parameters.

Model Size	$n_{\text{head}}$	Depth	Hidden dim	Params (M)
Small	8	8	640	44.98
Medium	8	12	784	92.78
Large	8	16	1024	214.61

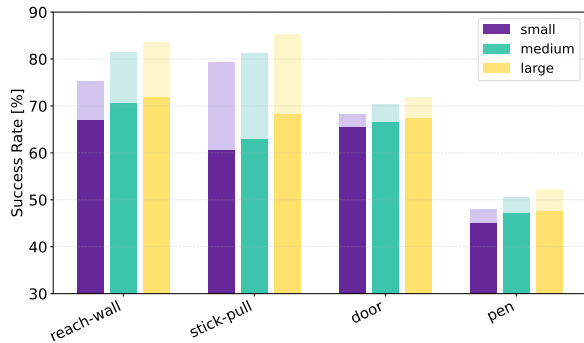


Fig. 6: **Scalability Study of ISS Policy with DiT model size.** We visualize SR<sub>5</sub> on four tasks using three DiT policy heads from Table II, with light bars (w/ ISS) and dark bars (w/o ISS).

actions. In contrast, enabling schedule sampling on top of ISS stabilizes this auxiliary supervision under model-predicted actions and mitigates exposure bias, yielding the best performance. Together, these modules are complementary: conditional fusion refines perception–action coupling; ISS shapes future-aware context representations; and schedule sampling makes this supervision effective under the model’s own action distribution, thereby improving robustness when rolling out the learned policy.

TABLE III: **Scalability Study of demonstration numbers.** We evaluate SR<sub>5</sub> of ISS Policy under different numbers of demonstrations on three tasks.

# Demos	Door	Pen	Reach-Wall	Average
10	72.0±2.0	52.3±2.7	83.7±1.3	69.3
30	73.8±6.8	69.0±6.0	85.0±4.0	75.9
50	80.8±0.8	83.3±2.8	87.0±3.0	83.7

TABLE IV: **Ablation on Designed Module.** We evaluate the effectiveness of Conditional Fusion, ISS Loss, and Schedule Sampling, reporting the average success rates on Adroit and MetaWorld.

Modules			Success Rate	
Cond. Fusion	ISS Loss	Schedule Samp.	Adroit	MetaWorld
✗	✗	✗	69.30	85.00
✓	✗	✗	70.77	87.78
✓	✓	✗	70.83	89.33
✓	✓	✓	74.77	91.68

**Impact of ISS Weight.** As shown in Table V, the performance peaks at ISS weight  $\lambda_{iss} = 0.4$ , achieving the highest average success rate of **89.75%**. While increasing the weight from 0.2 to 0.4 improves the results, further increasing it beyond this point leads to a gradual decline in performance. This indicates that a moderate weight strikes the optimal balance, providing sufficient geometric supervision to structure the feature space without interfering with the primary policy learning objective.

**Impact of Different Skip Steps.** As shown in Fig. 7, ISS Policy achieves highest performance under moderate skip lengths and prediction horizons. Compared to short-step prediction with  $K = 1$ , using a moderate skip ( $K = 2 \sim 4$ ) encourages the ISS head to forecast more pronounced

TABLE V: **Ablation on ISS loss weight  $\lambda_{iss}$ .** We compare different ISS loss weight across four tasks.

ISS Weight	Disassemble	Reach-Wall	Stick-Pull	Pick-Place-Wall	Average
0.2	87	82	82	85	84.00
0.4	<b>93</b>	<b>85</b>	<b>90</b>	91	<b>89.75</b>
0.6	92	83	82	<b>93</b>	87.50
0.8	91	77	87	89	86.00
1.0	<b>93</b>	80	78	90	85.25

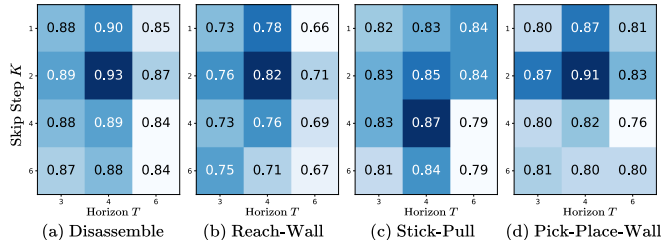


Fig. 7: **Ablation on Skip Step  $K$ .** We compare skip step with different prediction horizon across four tasks.

geometric changes, yielding richer geometric supervision and boosting success rates by roughly 2~5 percentages. In contrast, when the skip becomes too large (e.g.,  $K = 6$ ) or the prediction horizon is overly extended (e.g.,  $T = 6$ ), performance consistently degrades across tasks, suggesting that predicting scenes that are too far into the future makes the auxiliary task unnecessarily difficult and noisy, thereby weakening its beneficial effect on the action decoder.

### E. Real-World Experiments

**Experiment Settings.** The ISS policy was evaluated on an AgileX Piper robot by performing a cup-stacking task. Real-world visual observations were captured using a single Intel RealSense D455 camera, and the model was deployed for on-robot action inference on an NVIDIA RTX 4060 GPU. Our real-world setup and task procedure are shown in Figure 8. In cup-stacking task, the robot needs to precisely grasp the red cup and correctly stack it onto the blue cup. Real-world expert demonstrations were collected via teleoperation, yielding 50 trajectories for training.

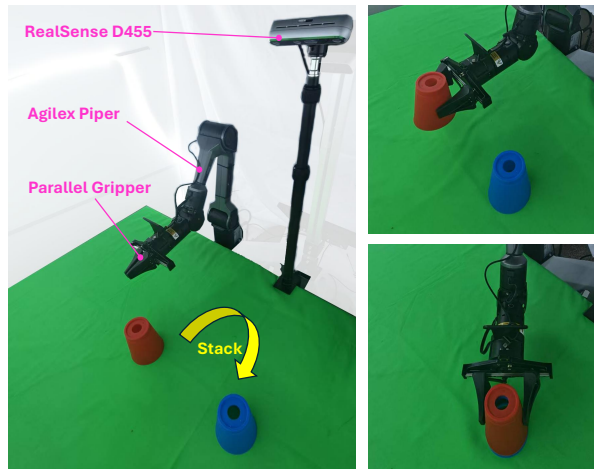


Fig. 8: **Real-World Experiment Setup.**

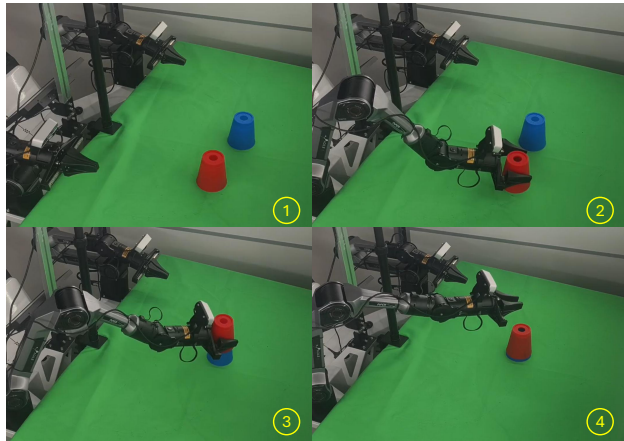


Fig. 9: **Real-World Experiments.** The image sequence illustrates the robot successfully grasping and stacking the cups, validating the effectiveness of ISS Policy in real-world manipulation tasks.

**Results.** As shown in Fig. 9, ISS Policy successfully grasps the red cup and stacks it onto the blue cup, demonstrating both accuracy and efficiency. On the real robot, the average inference time of DP3 is **161.4 ms**, while ISS Policy achieves **52.7 ms**, approximately 3× faster inference speed than DP3.

## VI. CONCLUSIONS

In this work, we propose **ISS Policy**, a DiT-based 3D visuomotor policy that is scalable and can be trained efficiently and stably. By further introducing a skip-step implicit scene supervision module that predicts future point-cloud features, we encourage the policy outputs to be inherently consistent with the geometric evolution of the scene. Notably, ISS Policy achieves state-of-the-art performance on dexterous hand manipulation (Adroit) and diverse single-arm manipulation tasks (MetaWorld), and exhibits strong robustness in real-world experiments.

## REFERENCES

- [1] S. Levine, C. Finn, T. Darrell, and P. Abbeel, “End-to-end training of deep visuomotor policies,” *Journal of Machine Learning Research*, vol. 17, no. 39, pp. 1–40, 2016.
- [2] T. Zhang, Z. McCarthy, O. Jow, D. Lee, X. Chen, K. Goldberg, and P. Abbeel, “Deep imitation learning for complex manipulation tasks from virtual reality teleoperation,” in *2018 IEEE international conference on robotics and automation (ICRA)*. Ieee, 2018, pp. 5628–5635.
- [3] F. Codevilla, M. Müller, A. López, V. Koltun, and A. Dosovitskiy, “End-to-end driving via conditional imitation learning,” in *2018 IEEE international conference on robotics and automation (ICRA)*. IEEE, 2018, pp. 4693–4700.
- [4] P. Florence, L. Manuelli, and R. Tedrake, “Self-supervised correspondence in visuomotor policy learning,” *IEEE Robotics and Automation Letters*, vol. 5, no. 2, pp. 492–499, 2019.
- [5] C. Chi, Z. Xu, S. Feng, E. Cousineau, Y. Du, B. Burchfiel, R. Tedrake, and S. Song, “Diffusion policy: Visuomotor policy learning via action diffusion,” *The International Journal of Robotics Research*, vol. 44, no. 10-11, pp. 1684–1704, 2025.
- [6] P. Florence, C. Lynch, A. Zeng, O. A. Ramirez, A. Wahid, L. Downs, A. Wong, J. Lee, I. Mordatch, and J. Tompson, “Implicit behavioral cloning,” in *Conference on robot learning*. PMLR, 2022, pp. 158–168.

- [7] A. Mandlekar, D. Xu, J. Wong, S. Nasiriany, C. Wang, R. Kulkarni, L. Fei-Fei, S. Savarese, Y. Zhu, and R. Martín-Martín, “What matters in learning from offline human demonstrations for robot manipulation,” *arXiv preprint arXiv:2108.03298*, 2021.
- [8] Y. Ze, G. Zhang, K. Zhang, C. Hu, M. Wang, and H. Xu, “3d diffusion policy: Generalizable visuomotor policy learning via simple 3d representations,” *arXiv preprint arXiv:2403.03954*, 2024.
- [9] M. Shridhar, L. Manuelli, and D. Fox, “Perceiver-actor: A multi-task transformer for robotic manipulation,” in *Conference on Robot Learning*. PMLR, 2023, pp. 785–799.
- [10] A. Goyal, J. Xu, Y. Guo, V. Blukis, Y.-W. Chao, and D. Fox, “Rvt: Robotic view transformer for 3d object manipulation,” in *Conference on Robot Learning*. PMLR, 2023, pp. 694–710.
- [11] Y. Chen, Y. Lin, R. Xu, and P. Vela, “Keypoint-graspnet: Keypoint-based 6-dof grasp generation from the monocular rgb-d input,” *arXiv preprint arXiv:2209.08752*, 2022.
- [12] Y. Ze, N. Hansen, Y. Chen, M. Jain, and X. Wang, “Visual reinforcement learning with self-supervised 3d representations,” *IEEE Robotics and Automation Letters*, vol. 8, no. 5, pp. 2890–2897, 2023.
- [13] J. Ho, A. Jain, and P. Abbeel, “Denoising diffusion probabilistic models,” *Advances in neural information processing systems*, vol. 33, pp. 6840–6851, 2020.
- [14] T. Osa, J. Pajarinen, G. Neumann, J. A. Bagnell, P. Abbeel, J. Peters, et al., “An algorithmic perspective on imitation learning,” *Foundations and Trends® in Robotics*, vol. 7, no. 1-2, pp. 1–179, 2018.
- [15] S. Haldar, J. Pari, A. Rai, and L. Pinto, “Teach a robot to fish: Versatile imitation from one minute of demonstrations,” *arXiv preprint arXiv:2303.01497*, 2023.
- [16] M. Reuss, Ö. E. Yağmurlu, F. Wenzel, and R. Lioutikov, “Multimodal diffusion transformer: Learning versatile behavior from multimodal goals,” *arXiv preprint arXiv:2407.05996*, 2024.
- [17] S. Liu, L. Wu, B. Li, H. Tan, H. Chen, Z. Wang, K. Xu, H. Su, and J. Zhu, “Rdt-1b: a diffusion foundation model for bimanual manipulation,” *arXiv preprint arXiv:2410.07864*, 2024.
- [18] Z. Gong, P. Ding, S. Lyu, S. Huang, M. Sun, W. Zhao, Z. Fan, and D. Wang, “Carp: Visuomotor policy learning via coarse-to-fine autoregressive prediction,” in *Proceedings of the IEEE/CVF International Conference on Computer Vision*, 2025, pp. 13 460–13 470.
- [19] H. Zhu, Y. Wang, D. Huang, W. Ye, W. Ouyang, and T. He, “Point cloud matters: Rethinking the impact of different observation spaces on robot learning,” *Advances in Neural Information Processing Systems*, vol. 37, pp. 77 799–77 830, 2024.
- [20] C. Wang, H. Fang, H.-S. Fang, and C. Lu, “Rise: 3d perception makes real-world robot imitation simple and effective,” in *2024 IEEE/RSJ International Conference on Intelligent Robots and Systems (IROS)*. IEEE, 2024, pp. 2870–2877.
- [21] T. Gervet, Z. Xian, N. Gkanatsios, and K. Fragkiadaki, “Act3d: 3d feature field transformers for multi-task robotic manipulation,” *arXiv preprint arXiv:2306.17817*, 2023.
- [22] T.-W. Ke, N. Gkanatsios, and K. Fragkiadaki, “3d diffuser actor: Policy diffusion with 3d scene representations,” *arXiv preprint arXiv:2402.10885*, 2024.
- [23] T. Chen, Y. Mu, Z. Liang, Z. Chen, S. Peng, Q. Chen, M. Xu, R. Hu, H. Zhang, X. Li, et al., “G3flow: Generative 3d semantic flow for pose-aware and generalizable object manipulation,” in *Proceedings of the Computer Vision and Pattern Recognition Conference*, 2025, pp. 1735–1744.
- [24] J. Song, C. Meng, and S. Ermon, “Denoising diffusion implicit models,” *arXiv preprint arXiv:2010.02502*, 2020.
- [25] Y. Song, J. Sohl-Dickstein, D. P. Kingma, A. Kumar, S. Ermon, and B. Poole, “Score-based generative modeling through stochastic differential equations,” *arXiv preprint arXiv:2011.13456*, 2020.
- [26] R. Rombach, A. Blattmann, D. Lorenz, P. Esser, and B. Ommer, “High-resolution image synthesis with latent diffusion models,” in *Proceedings of the IEEE/CVF conference on computer vision and pattern recognition*, 2022, pp. 10 684–10 695.
- [27] Z. Xian, N. Gkanatsios, T. Gervet, T.-W. Ke, and K. Fragkiadaki, “Chaineddiffuser: Unifying trajectory diffusion and keypose prediction for robotic manipulation,” in *7th Annual Conference on Robot Learning*, 2023.
- [28] J. Cao, Q. Zhang, J. Sun, J. Wang, H. Cheng, Y. Li, J. Ma, K. Wu, Z. Xu, Y. Shao, et al., “Mamba policy: Towards efficient 3d diffusion policy with hybrid selective state models,” *arXiv preprint arXiv:2409.07163*, 2024.
- [29] S. Yan, Z. Zhang, M. Han, Z. Wang, Q. Xie, Z. Li, Z. Li, H. Liu, X. Wang, and S.-C. Zhu, “M 2 diffuser: Diffusion-based trajectory optimization for mobile manipulation in 3d scenes,” *IEEE Transactions on Pattern Analysis and Machine Intelligence*, 2025.
- [30] T. Wu, M. Wu, J. Zhang, Y. Gan, and H. Dong, “Learning score-based grasping primitive for human-assisting dexterous grasping,” *Advances in Neural Information Processing Systems*, vol. 36, pp. 22 132–22 150, 2023.
- [31] J. Urain, N. Funk, J. Peters, and G. Chalvatzaki, “Se (3)-diffusionfields: Learning smooth cost functions for joint grasp and motion optimization through diffusion,” in *2023 IEEE International Conference on Robotics and Automation (ICRA)*. IEEE, 2023, pp. 5923–5930.
- [32] K. R. Barad, A. Orsula, A. Richard, J. Dentler, M. A. Olivares-Mendez, and C. Martinez, “Graspldm: Generative 6-dof grasp synthesis using latent diffusion models,” *IEEE Access*, vol. 12, pp. 164 621–164 633, 2024.
- [33] Z. Weng, H. Lu, D. Kragic, and J. Lundell, “Dexdiffuser: Generating dexterous grasps with diffusion models,” *IEEE Robotics and Automation Letters*, 2024.
- [34] A. Sridhar, D. Shah, C. Glossop, and S. Levine, “Nomad: Goal masked diffusion policies for navigation and exploration,” in *2024 IEEE International Conference on Robotics and Automation (ICRA)*. IEEE, 2024, pp. 63–70.
- [35] W. Cai, J. Peng, Y. Yang, Y. Zhang, M. Wei, H. Wang, Y. Chen, T. Wang, and J. Pang, “Navdp: Learning sim-to-real navigation diffusion policy with privileged information guidance,” *arXiv preprint arXiv:2505.08712*, 2025.
- [36] S. Samavi, A. Lem, F. Sato, S. Chen, Q. Gu, K. Yano, A. P. Schoellig, and F. Shkurti, “Sicnav-diffusion: Safe and interactive crowd navigation with diffusion trajectory predictions,” *IEEE Robotics and Automation Letters*, 2025.
- [37] W. Peebles and S. Xie, “Scalable diffusion models with transformers,” in *Proceedings of the IEEE/CVF international conference on computer vision*, 2023, pp. 4195–4205.
- [38] A. Ramesh, P. Dhariwal, A. Nichol, C. Chu, and M. Chen, “Hierarchical text-conditional image generation with clip latents,” *arXiv preprint arXiv:2204.06125*, vol. 1, no. 2, p. 3, 2022.
- [39] A. Vaswani, N. Shazeer, N. Parmar, J. Uszkoreit, L. Jones, A. N. Gomez, Ł. Kaiser, and I. Polosukhin, “Attention is all you need,” *Advances in neural information processing systems*, vol. 30, 2017.
- [40] P. Li and D. Cui, “Navigation-guided sparse scene representation for end-to-end autonomous driving,” *arXiv preprint arXiv:2409.18341*, 2024.
- [41] S. Bengio, O. Vinyals, N. Jaitly, and N. Shazeer, “Scheduled sampling for sequence prediction with recurrent neural networks,” *Advances in neural information processing systems*, vol. 28, 2015.
- [42] A. Rajeswaran, V. Kumar, A. Gupta, G. Vezzani, J. Schulman, E. Todorov, and S. Levine, “Learning complex dexterous manipulation with deep reinforcement learning and demonstrations,” *arXiv preprint arXiv:1709.10087*, 2017.
- [43] T. Yu, D. Quillen, Z. He, R. Julian, K. Hausman, C. Finn, and S. Levine, “Meta-world: A benchmark and evaluation for multi-task and meta reinforcement learning,” in *Conference on robot learning*. PMLR, 2020, pp. 1094–1100.
- [44] Y. Seo, D. Hafner, H. Liu, F. Liu, S. James, K. Lee, and P. Abbeel, “Masked world models for visual control,” in *Conference on Robot Learning*. PMLR, 2023, pp. 1332–1344.
- [45] C. Wang, X. Luo, K. Ross, and D. Li, “Vrl3: A data-driven framework for visual deep reinforcement learning,” *Advances in Neural Information Processing Systems*, vol. 35, pp. 32 974–32 988, 2022.